Scalable Synthesis of 2D Hydrogen-Substituted Graphdiyne on Zn Substrate for High-Yield N₂ Fixation

Qi Yang^{1‡}, Ying Guo^{1‡}, Jinxing Gu^{2‡}, Na Li¹, Changda Wang³, Zhuoxin Liu¹, Xinliang Li¹, Zhaodong Huang¹, Shiqiang Wei³, Suying Xu⁴, Li Song³, Jun Fan^{1*}, Zhongfang Chen^{2*}, Jieshan Qiu⁴, and Chunyi Zhi^{1,5*}

- ³ National Synchrotron Radiation Laboratory CAS Center for Excellence in Nanoscience, University of Science and Technology of China, Hefei 230029, China
- ⁴ State Key Laboratory of Chemical Resource Engineering, Beijing University of Chemical Technology, Beijing 100029, China

¹ Department of Materials Science and Engineering, City University of Hong Kong, 83 Tat Chee Avenue, Hong Kong SAR 999077, China

² Department of Chemistry, University of Puerto Rico, Rio Piedras Campus, San Juan, PR, 00931, USA

⁵ Shenzhen Research Institute, City University of Hong Kong, Shenzhen 518057, China.

[‡]These authors contributed equally.

^{*} E-mail: junfan@cityu.edu.hk; zhongfangchen@gmail.com; cy.zhi@cityu.edu.hk

Abstract

Hydrogen-substituted graphdiyne (HsGDY), as a new rising star of carbon materials family, demonstrates high conjugation, robust chemical stability, and versatility for modification. However, grand challenges, including low production rate, disordered topology, and amorphous structure, greatly hinder its large-scale applications. Herein, we report, for the first time, the scalable synthesis (up to gram-level) of two-dimensional (2D) crystalline HsGDY nanosheets with Zn as a substrate. Moreover, as a metal-free catalyst for electrochemical N₂ fixation, 2D HsGDY achieves an ultrahigh yield of 103 μg h⁻¹ mg⁻¹_{cat.} with a potential of -0.2 V vs reversible hydrogen electrode (RHE), which is comparable with that of noble metals and single-atom catalysts. Different from the heteroatom active sites in carbon-based catalysts reported before, the inner alkynyl C itself in 2D HsGDY was identified as the active site, which adsorbs and activates N≡N due to the positive charge and high spin density triggered by the slight O doping in the form of C=O at the outer alkynyl C. We believe that this Zntemplated scalable production of high-quality HsGDY paves the way for its large-scale production and provides a new playground for the multiple research fields.

Keywords: graphdiyne; zinc substrate; two dimensional; N₂ fixation; electron delocalization

Introduction

Since the first synthesis in 2010 by Li and coworkers¹, graphdiyne (GDY), a new carbon nanomaterial constructed by the periodic distribution of benzene ring and alkynyl, experienced dramatic advances from theoretical prediction to practical applications²⁻⁴. The intrinsic structure traits of sp- and sp²-hybridized carbon atoms bring GDY unique properties, such as feasible chemical tailorability at alkynyl sites, highly-ordered pore structure, extended π -conjugation, and controllable band gap⁵. These properties endow GDY with promising applications in numerous and diverse fields, such as catalysis⁶, energy⁷, sensor⁸, medicine⁹, and environment¹⁰, which in turn encourage the progress in further advancing GDY and its analogues. Along this line, He et al. synthesized hydrogen-substituted graphdiyne (HsGDY), the first derivative of GDY developed to increase the capability of lithium/sodium ion storage¹¹. The introduced H atoms occupy three septal sites of benzene in 1,3,5-Triethynylbenzene (TEB) monomer, and thus well separate three acetenyls, generating the HsGDY network. Interestingly, Lv et al. selectively doped nitrogen into HsGDY through substituting the carbon atoms in a benzene ring by N atoms, and demonstrated that the as-synthesized pyridinic nitrogen-doped HsGDY is a superior metal-free catalyst for oxygen reduction¹².

Note that all the HsGDYs reported so far were synthesized on Cu foils. These HsGDYs are of either porous network/particle morphology or amorphous crystalline structures¹¹⁻¹⁴. Such structural features seriously deviate from the ideal ordered 2D materials and suggest the spatially unordered cross-coupling reactions between adjacent TEB monomers. This phenomenon is partially attributed to the non-coplanar polymerization due to the linear rotation along the butadiyne.¹⁵ Moreover, the synthesis of high-quality HsGDY still suffers from the issue of low production rate, and its large-scale application is not practical. Clearly, a facile fabrication protocol, which can realize scalable preparation of HsGDY with high quality, will greatly boost our understanding of HsGDY and achieve its large-scale applications.

Herein, guided by density functional theory (DFT) computations, we find Zn, adjacent to Cu in the Periodic Table, is a highly efficient substrate for scalable synthesis of 2D crystalline HsGDY. The Zn-templated HsGDY possesses a 2D morphology with micron-level lateral size, bilayer thickness, and high crystallinity, implying the highly ordered monomer polymerization process. Using Zn as substrate, we obtained HsGDY with the mass of up to 0.5 g, which paves the way for the large-scale applications in energy storage and catalysis. These advantages encourages us to investigae the assynthesized HsGDY as catalysts of the electrochemical N₂ reduction reaction (NRR), which has been regarded as a highly promising protocol for ammonia synthesis because of the competitive raw ingredients (water and air) and driving force (renewable solar and wind energy)^{16, 17}. We demonstrate that the as-synthesized HsGDY is an outstanding metal-free NRR catalyst, achieving an ultrahigh yield of 103 μg h⁻¹ mg⁻¹cat. with an optimal potential of -0.2 V vs reversible hydrogen electrode (RHE), which is comparable with the top-level single-atom catalysts and far surpasses other carbonbased and metal oxide catalysts, ¹⁸⁻²³. DFT computations reveals that the inner alkynyl C atoms close to the oxygen dopants are active sites. This work represents great advances in both synthesis of high-quality HsGDY and its application in high-yield N₂ fixation as a metal-free catalyst.

Results and discussion

Searching for an appropriate substrate to grow highly crystalline HsGDY. Note that in previous syntheses of HsGDY and its analogues, Cu foil is dominantly employed as substrate which directs the cross-coupling reaction on the solid-liquid interface. However, with only a single electron at its outermost 4s orbital, Cu is expected to trigger strong interactions between the singly occupied Cu 4s electron orbital and the alkynyl π electrons of TEB monomer ²⁴. This speculation is verified by our DFT computations: when TEB is adsorbed on the Cu catalytic substrate, significant charge transfer occurs as revealed by the deformation charge density, and the alkynyls deviate from the benzene ring plane substantially (Fig. 1a, 1c, and S1). This non-coplanar configuration will lead to the disordered cross-coupling of TEB monomer and result in the particle

morphology or the amorphous structure. It is the electron-unsaturated nature of Cu catalytic substrate that causes the monomer configuration distortion. Thus, it is likely to grow 2D crystalline HsGDY on a more suitable substrate that possesses appropriate interaction energies with the precursors ²⁵⁻²⁷. This finding inspires and guides us to find a new substrate of electron-saturated Zn to address the morphology and structure issues faced by current HsGDY community.

DFT computations show that on the Zn (001) plane, TEB well maintains its planar configuration with an alkynyl-substrate distance of 2.944 Å, and its binding energy with the Zn substrate (-1.53 eV) is also much less than that on Cu (-2.07 eV) (Fig. 1b). Such differences can be understood by the more pronounced charge transfer between TEB and Cu substrate (Fig. 1c and 1d). Therefore, Zn is expected to serve as a suitable substrate to synthesize crystalline HsGDY.

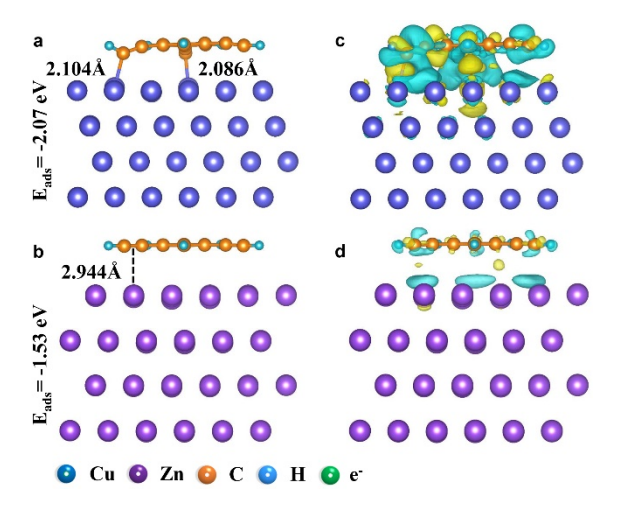


Fig. 1. Monomer molecule configuration on Cu and Zn substrates. a and b, Optimized structure of TEB on Cu (a) and Zn (b) substrates, showing the molecule configuration. **c and d**, Deformation charge density of TEB/Cu (c) and TEB/Zn (d), demonstrating the vertical charge transfer between TEB and substrates.

Morphology characterizations. HsGDY is prepared by solid-liquid interface polymerization of TEB monomer based on the alkynyl-site cross-coupling reaction templated by Zn substrate, in comparison with Cu substrate.

Scanning electron microscopy (SEM) image reveals that HsGDY formed on Cu substrate consists of enormous particles with quasi-nanoscale diameter (Fig. 2a and S2a). Transmission electron microscopy (TEM) image confirms the particle morphology and highlights the apparent nanogaps between adjacent particles (Fig. 2b and S2b). The amorphous feature of HsGDY is uncovered by high resolution TEM (HRTEM) (Fig. 2c).

The morphology and the crystalline structure of HsGDY synthesized on Zn substrate are totally different. SEM image shows a nanosheet morphology and a microns-level lateral size of HsGDY (Fig. 2d). To the best of our knowledge, this is the first demonstration of 2D crystalline HsGDY nanosheet as predicted by theoretical simulation based on the coplanar cross-coupling. 14, 28 These HsGDY nanosheets are observed to be semi-transparent in the TEM image, further verifying the nanosheet morphology and the ultrathin thickness (Fig. 2e). Accompanied by the 2D morphology, HRTEM image detects, for the first time, the clear lattice diffraction fringe with an interlayer spacing of 0.361 nm, which suggests the high crystallinity (Fig. 2f). The corresponding selected area electron diffraction (SAED) image reveals the polycrystalline feature of Zn-templated HsGDY compared with the amorphous HsGDY synthesized on Cu substrate (Fig. S3). Atomic force microscope (AFM) image together with the height-length profiles reveals the ultrathin thickness of 0.68-0.75 nm, corresponding to a bilayer HsGDY (Fig. 2g-2i).

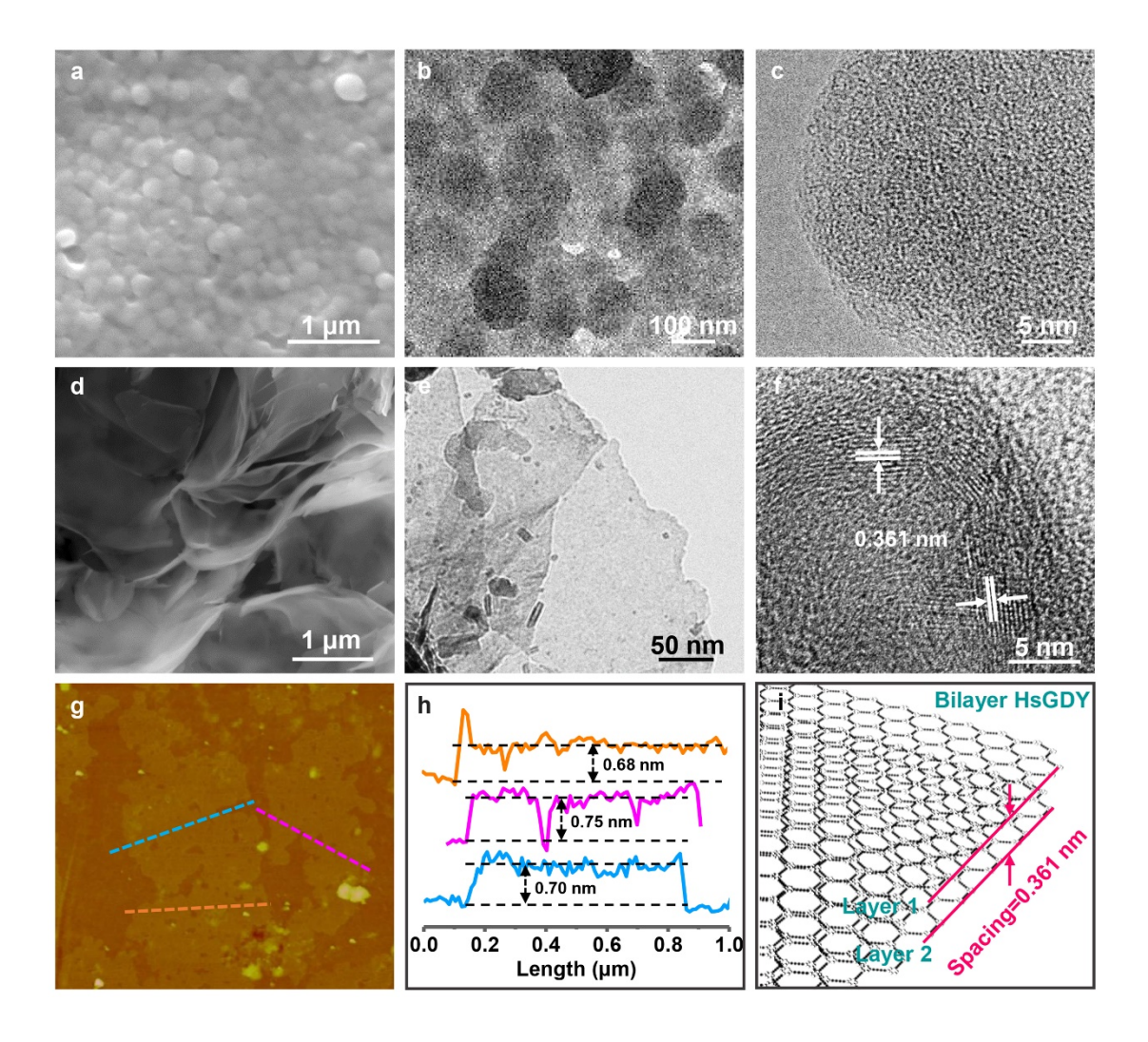


Fig. 2. First demonstration of 2D HsGDY with high crystallinity and bilayer thickness. a-c, SEM image (a), TEM image (b), and HRTEM image (c) of the HsGDY synthesized on Cu substrate. d-f, SEM image (d), TEM image (e), and HRTEM image (f) of the HsGDY synthesized on the Zn substrate. g-i, AFM image (g), the corresponding height-length profiles (h), and schematic diagram (i) of the HsGDY synthesized on Zn substrate.

Spectroscopy analyses of the chemical structure. The digital image shows the color evolution from argentite to light yellow before and after HsGDY formation (Fig. 3ai). The HsGDY interface network features the alternate distribution of benzene ring and alkynyl as the building units, and is formed by the alkynyl-site cross-coupling reaction (Fig. 3aii) ^{29, 30}. It should be noted that this schematic diagram (Fig. 3aii) exhibits the ideal structure of HsGDY without oxygen dopants to make it easy for readers to

understand the backbone of HsGDY, while the actual chemical structures of HsGDY with oxygen dopants will be discussed in the following contents.

As one of the key approaches to investigate HsGDY, Raman spectra collected at three different points exhibit the characteristic peaks of benzene ring (1584 cm⁻¹), alkynyl (1931, 2188 cm⁻¹), and defect (1352 cm⁻¹), demonstrating the as-predicted polymerization of TEB monomers on Zn substrate to form HsGDY (Fig. 3b and S4) ³¹, ³². Accordingly, Raman mappings targeting the alkynyl and benzene ring in HsGDY demonstrate the homogeneous distribution of both functional groups along the 2D surface (Fig. 3c and 3d). Fourier transform infrared spectroscopy (FTIR) spectrum shows apparent adsorption peaks of C-C (benzene ring 1490-1700 cm⁻¹, alkynyl 2191-2450 cm⁻¹), C-H (stretching vibration 2972-3200 cm⁻¹, bending vibration 845-951 cm⁻¹), and C=O (carbonyl stretching 1680-2000 cm⁻¹) bonds (Fig. 3e)^{33, 34}.

We further use X-ray technologies, including X-ray photoelectron spectroscopy (XPS) and X-ray absorption near edge spectroscopy (XANES), to further examine the fine chemical circumstance of HsGDY. The survey XPS spectra (Fig. 3e) exhibit the remarkable presence of C element (*ca.* 280-290 eV) and the coexistence of Zn element (1020 and 1040 eV) after HsGDY formation, further evidencing the expected synthesis of HsGDY on Zn substrate (Fig. 3f). High-resolution C1s XPS spectrum confirms the dominant presence of benzene rings (C=C, 284.6 eV) and alkynyl groups (C=C, 285.4 eV) (Fig. 3g).

In addition, trace amount of oxygen (C-O at 288 eV, C=O at 289.6 eV) are also detected due to the weak oxidation at the alkynyl site 35 . High-resolution O1s spectrum indexes the oxygen to carbonyl (C=O, 531.6 eV), ester (O=C-O, 532.6 eV), and hydroxy (O-H, 533.7 eV) (Fig. S5) 36 . With higher precision, C K-edge XANES (Fig. 3h) further confirms HsGDY's chemical environment: C=C bond (benzene ring, 285.1 and 292.9 eV for π and σ excitations respectively), C=C bond (285.6 eV, as magnified in the inset), C=O/C-O bond (288.6 eV), C-H bond (290.4 eV) $^{37, 38}$. Other than confirming the carbon-based chemical structures, these multiple spectroscopy analyses

consistently detect the presence of oxygen dopants with the form of C=O/C-O, which is expected to subtly mediate the localized electronic structures and thus affect the catalytic performance.

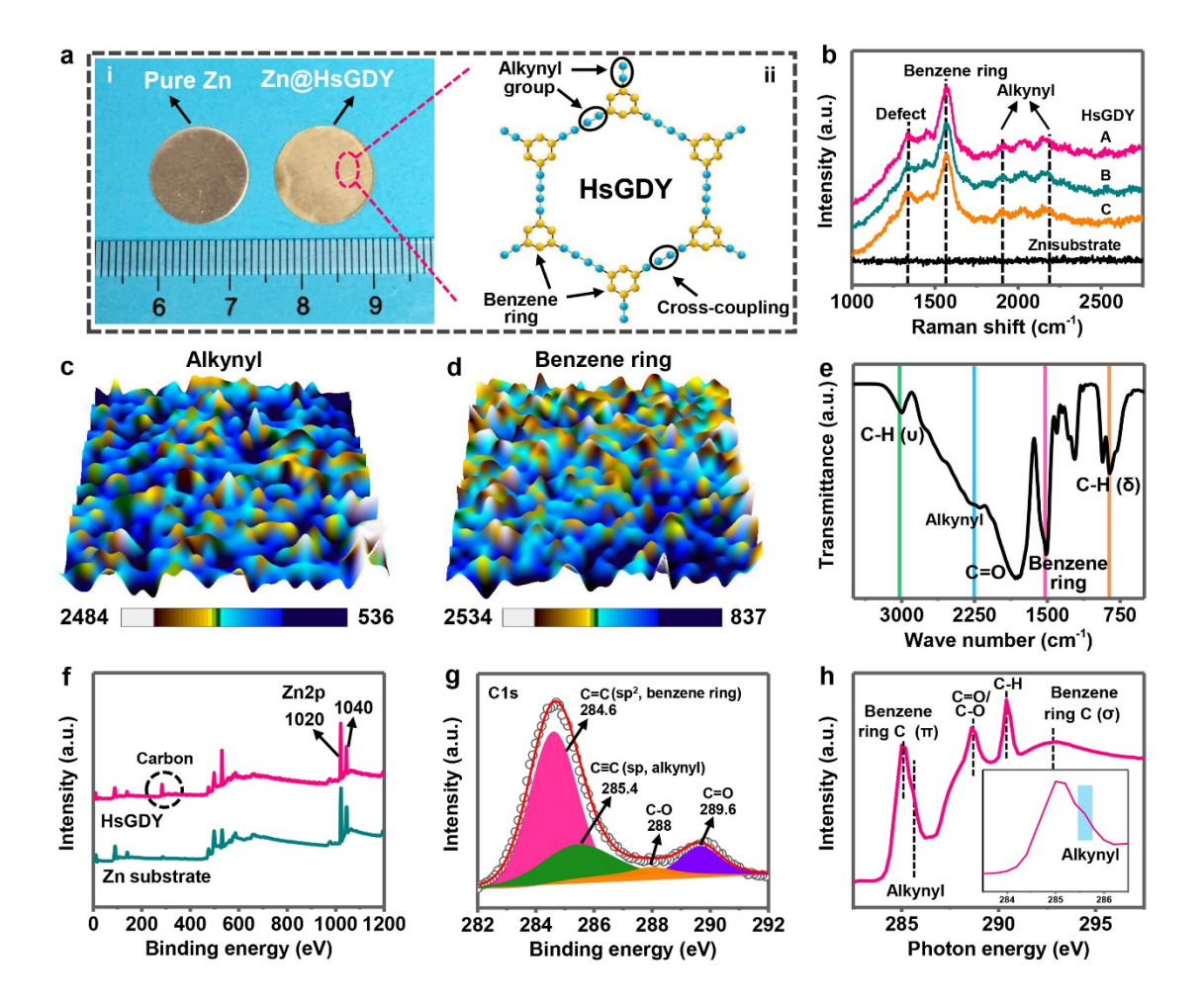
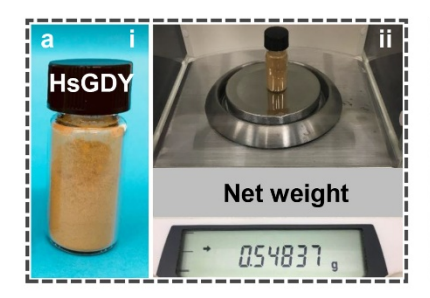
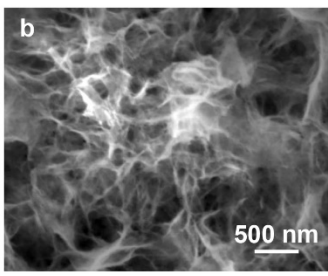


Fig. 3. Spectroscopy analyses of the chemical structure of HsGDY. a, Digital image of commercial Zn foil and HsGDY@Zn (i) and the corresponding schematic illustration of HsGDY (ii). b, Raman spectra of Zn@HsGDY at three different detecting points (see Fig. S4). c and d, Raman mappings of HsGDY synthesized on Zn foil focused on Raman shifts of alkynyl (c) and benzene ring (d). e, FTIR of HsGDY showing the fingerprint peaks of C-C, C-H, and C=O bonds. f, g, XPS data of survey (f) and high-resolution C1s (g) spectra. h, C K-edge XANES of HsGDY revealing the chemical environment of C atoms. The inset shows the magnified peak of alkynyl.

Scalable synthesis of HsGDY. The low production rate of HsGDY and its analogues is another urgent issue. To conquer this challenge, we utilize Zn powder as the substrate

to direct the scalable synthesis of HsGDY. This process proceeds on the solid-liquid interface and generates enormous HsGDY as observed by the SEM images (Fig. S6a and S6b). The corresponding XPS survey spectrum confirm the removal of Zn powder substrate during the etching process (Fig. S6c). This interface reaction offers the possibility to address the scalable synthesis issue. Fig. 4a shows the scalable production of HsGDY (0.548 g). SEM and TEM images confirm the similar 2D nanosheet morphology with that prepared on Zn foil (Fig. 4b and 4c). The as-produced sample is examined to exhibit highly ordered pore size of 1-2.5 nm and a surface area of 220.9 m² g⁻¹ (Fig. S7). Another advantage of this synthetic method is the sustainability: the raw material (Zn) can be well recycled and reused: initially, Zn powder is used to catalyze HsGDY formation, and then etched away after the synthetic process; the generated Zn ion is electrochemically reduced back into metallic Zn to serve as the substrate in the next round synthesis (Fig. S8). This scalable yet green synthetic method paves the way for the large-scale application of HsGDY.





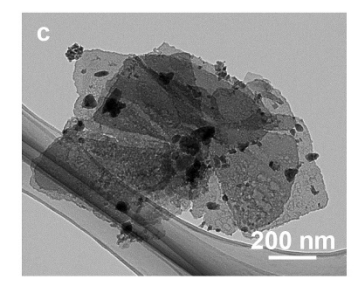


Fig. 4. Scalable synthesis of HsGDY. a, Digital images of HsGDY in vial (i) and the net weight (ii) showing the scalable synthesis. **b, c,** SEM image (**b**) and TEM image (**c**) demonstrate the 2D nanosheet topology.

Electrochemical N₂ fixation. Electrochemical nitrogen fixation at ambient conditions holds great promise for sustainably synthesizing ammonia, which is an essential building block for manufacturing synthetic chemicals and a promising green energy carrier to advance a low-carbon society ³⁹⁻⁴². We herein evaluate the N₂ fixation capability of the synthesized HsGDY, as a novel metal-free catalyst, in a N₂-saturated 0.05 M H₂SO₄ electrolyte within an H-shape configuration (as shown in Fig. S9)

according to a rigorous protocol ⁴³. Initially, Linear sweep voltammetric (LSV) examination is carried out in electrolytes saturated with N2 and Ar, respectively, to preliminarily evaluate the NRR catalytic activity of HsGDY (Fig. 5a). Apparently, the response current density in N2 is larger than that in Ar, especially within the potential range from -0.2 to -0.4 V, implying extra contribution from the NRR process ⁴⁴⁻⁴⁶. In addition, we also repeat the LSV examination for another two segments to confirm the reliability of the results ^{47, 48}. These three segments of LSV curves demonstrate good accordance with each other, excluding the influence of other experimental factors on NRR. Chronoamperometry curves are then recorded for 7200 s at different potentials ranging from -0.1 to -0.5 V, which demonstrate the desirable stability of HsGDY catalyst (Fig. 5b). The electrolytes containing (NH₄)₂SO₄ (originated from the reaction between NH₃ and H₂SO₄) after the electrochemical N₂ fixation are quantitatively detected by UV-Vis absorption spectra (Fig. 5c). Before this, the absorbanceconcentration linear relation is calibrated using standard (NH₄)₂SO₄ solution (Fig. S10). NH₃ yield rate, a crucial evaluation indicator of NRR capability, is calculated to reach the highest value (103 µg h⁻¹ mg⁻¹_{cat.}) at -0.2 V, which surpasses the majority of current NRR catalysts ranging from carbon-based catalysts (2.1-55 µg h⁻¹ mg⁻¹cat.) to noble metal and single-atom catalysts (1.6-34.8 μg h⁻¹ mg⁻¹_{cat.}) (Fig. 5d and Supplementary Table 1) ⁴⁹⁻⁵⁶. Correspondingly, the Faradic efficiency (FE, %) of NH₃ production also achieves the largest value of (5.13%) at -0.2 V due to the synergistic effect of favored NRR and suppressed hydrogen evolution reaction (Fig. 5e).

To verify that the detected NH₃ originates from the reduction of the bubbling N₂ by HsGDY, we perform the control experiment using pristine carbon cloth at -0.2 V and compare its performance with HsGDY catalyst at open-circuit voltage (OCV) (Fig. S11). In addition, we also examine the purity of the feeding gas, excluding the possible influence of NO_x on the NRR (Fig. S12). For the control experiment, the hydrazine byproduct is scarcely detected in the reacted electrolyte at the whole voltage range, which evidences the high selectivity of HsGDY (Fig. S13). To obtain a definite proof that the detected NH₃ is from the reduction of N₂ into NH₃ catalyzed by HsGDY, we

also perform the ¹H Nuclear Magnetic Resonance (NMR) experiments using both ¹⁴N₂ and ¹⁵N₂ gases. As shown in Fig. 5f, the signal of ¹⁴NH₃ and ¹⁵NH₃ are detected in the electrolytes after the NRR, which are in good accordance with the signal of the standard (¹⁴NH₄)₂SO₄ and (¹⁵NH₄)₂SO₄ solutions. Furthermore, we also carry out the quantitative NMR analysis and obtain the signal integration-concentration linear relation (Fig. 5g and 5h). The concentration of (NH₄)₂SO₄ is calculated to be 7.66 μM, which is consistent with the result of UV-Vis absorption spectra (7.70 μM), convincingly evidencing the reduction of N₂ into NH₃ catalyzed by HsGDY catalyst (Fig. 5i).

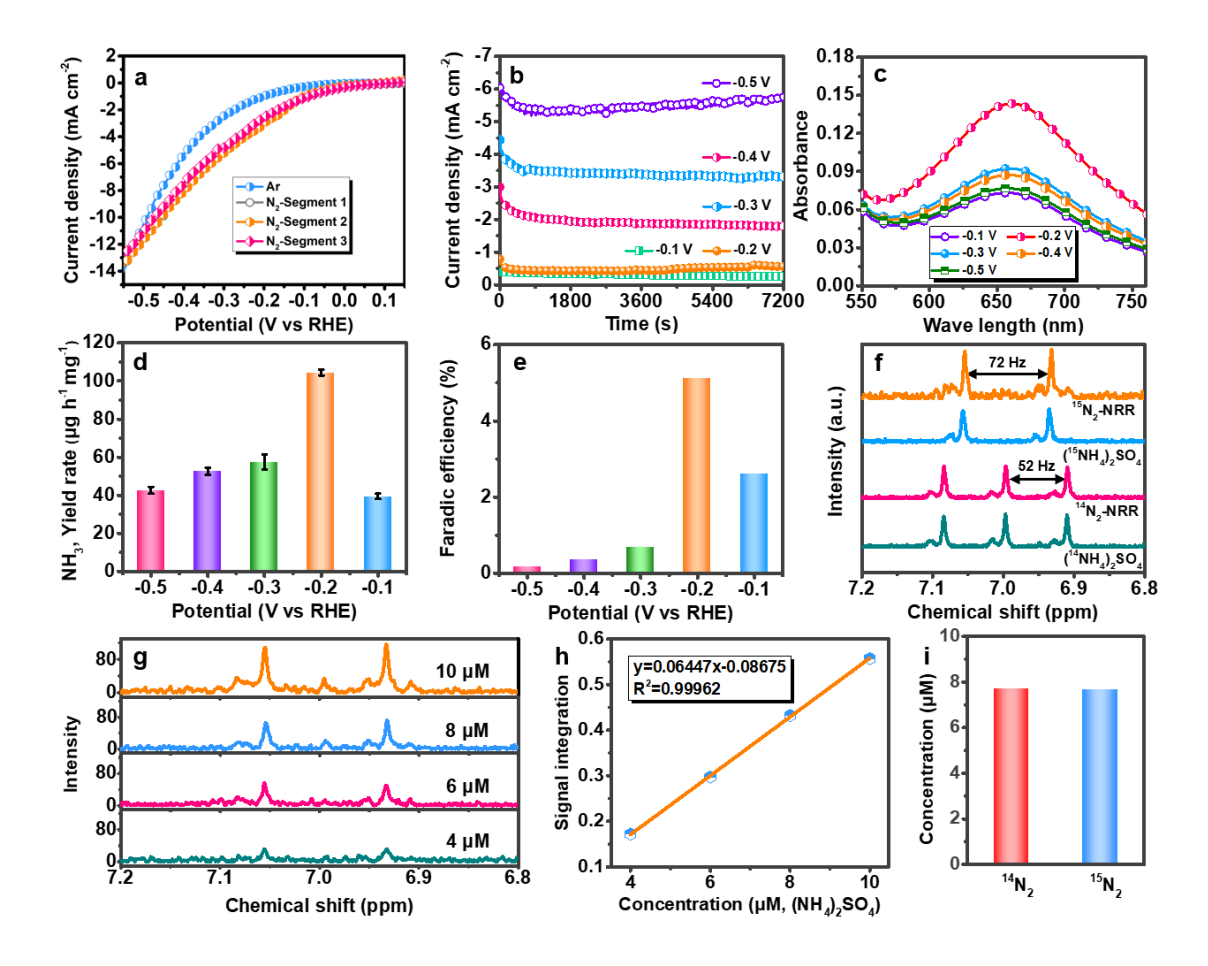


Fig. 5. Electrochemical N₂ fixation assessment. **a,** LSV examination in Ar and N₂ saturated electrolytes to evaluate the possible potential range for NRR. **b,** Current-time profiles obtained at various potentials from -0.1 to -0.5 V for calculating the whole charge quantity consumed. **c,** UV-Vis absorption spectra of electrolytes after NH₃ formation at different potentials. **d, e,** The calculated yield rate (**d)** of NH₃ at various potentials and the corresponding FE (**e)**. **f,** ¹H NMR spectra of electrolyte saturated with

¹⁵N₂ after NRR and standard (¹⁵NH₄)₂SO₄ solution. **g**, ¹H NMR spectra of standard (¹⁵NH₄)₂SO₄ solutions with different concentrations of 4-10 μM. **h**, Signal integration-concentration linear relation calibrated using standard (¹⁵NH₄)₂SO₄ solutions. **i**, Concentration of (NH₄)₂SO₄ in the electrolytes using ¹⁴N₂ and ¹⁵N₂ as feeding gases.

Identification of active site and catalytic mechanism. Our electrochemical measurements strongly confirm that the as-synthesized HsGDY has outstanding activity towards NRR. Is the NRR activity attributed to the pristine HsGDY itself or some dopants in HsGDY? To answer this question, we perform extensive DFT computations to screen out the active site and investigate the NRR mechanism.

Firstly, we examine the catalytic activity of pristine HsGDY towards NRR^{47,48}. Unfortunately, N₂ molecule cannot be activated on the pristine HsGDY due to weak physisorption (Fig. S14), thus the pristine HsDGY is not capable of catalyzing NRR.

Considering that carbonyl groups exist in all the synthesized HsGDY samples, as evidenced by XANES, XPS, and FTIR analyses, we systematically investigate the catalytic performance of various oxygen-doped HsGDY models, including three possible models with one oxygen atom interacting with the pristine HsGDY (Fig. S15) and eight models with broken carbon-carbon chains terminated with hydroxyl, carbonyl, aldehyde, and carboxyl groups (Fig. S16).

These extensive DFT computations screen out one O-doped HsGDY model, as presented in Fig. 6a, with catalytic performance compatible to our experiments. This model features a two-atom carbon chain terminated with an aldehyde group. We reveal that the activity of this model arises from the carbene-like active site, i.e, the inner alkynyl carbon atom, whose stability can be understood by the conjugation between this carbon atom and the adjacent carbon hexagonal ring. On this active site, NRR preferably proceeds through a mixed mechanism (Fig. 6a). Firstly, the outer nitrogen obtains two proton-electron pairs sequentially, followed by the similar hydrogenation process on the inner nitrogen atom. Then, the nitrogen-nitrogen bond is broken, leading to the release of the first ammonia. Subsequently, the remained *NH₂ species obtains

another proton-electron pair and converts to the second released ammonia. After examining the corresponding free energy profile of the elementary steps (Fig. 6b), we find that NRR cannot proceed at a zero potential on the active site due to the uphill energy steps, namely the formation of *NH₂NH₂ species and the formation of *NH₃ species. With the largest energy barrier (*ca.* 0.30 eV), the formation of *NH₂NH₂ is the potential determining step. Besides, this energy barrier is much lower than the other models (0.42-0.63 eV) (Fig. S17). At the limiting potential of – 0.30 V, all the NRR elementary steps possess negative or zero Gibbs free energy changes (except for the release of ammonia gas). The limiting potential (– 0.30 V) slightly differs the potential observed in our experiments (– 0.2 V) because of the simplified model with limited number of atoms. It has been widely reported that DFT calculations do reproduce the relative trend of catalytic activity observed in experiments ^{57,58}. Thus, we identify that the outstanding NRR performance of HsGDY can be ascribed to the alkynyl carbon atom itself (rather than the O dopant) between the carbon hexagonal ring and the aldehyde group.

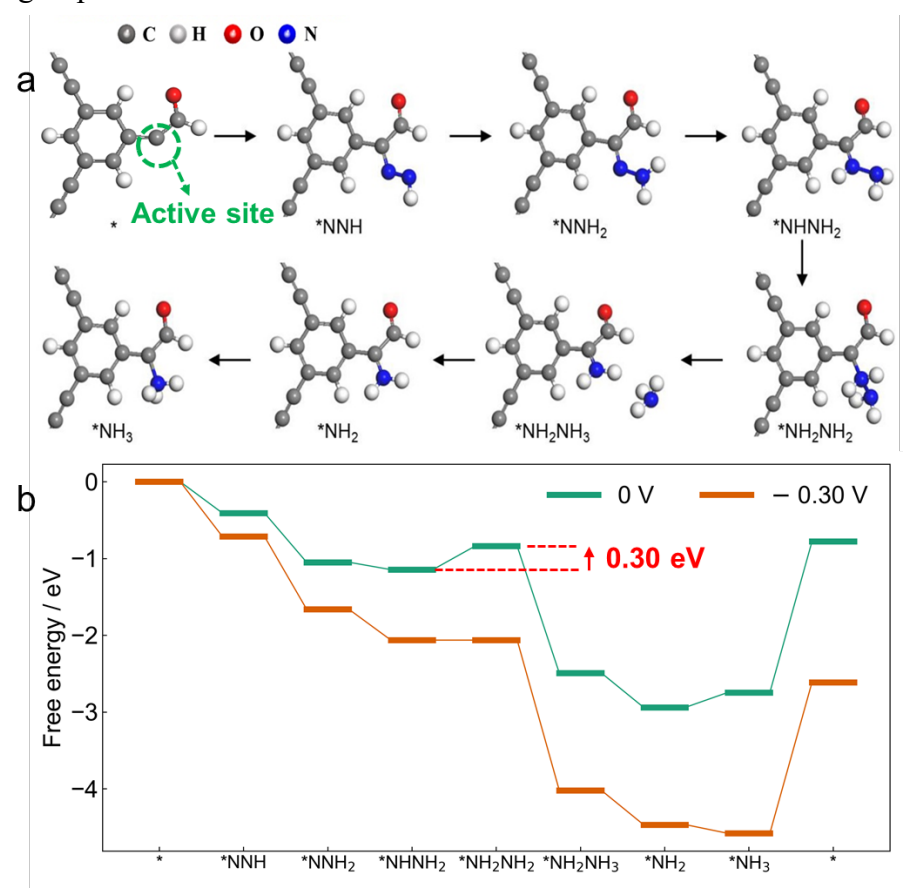


Fig. 6. Identification of active site and catalytic mechanism for NRR. (a) The identified mixed NRR mechanism on the screened model, where the active site is labeled. For simplicity, the catalyst itself is represented by asterisk (*), and the adsorbed N-containing species is named by joining the asterisk and its chemical formula together. (b) The free energy profile of various NRR elementary steps under zero and the limiting potentials, where the potential limiting step is marked in red.

Conclusion

In conclusion, guided by DFT computations, we present a protocol of using Zn (rather than the traditional Cu) as the substrate to grow planar crystalline HsGDY in a scalable manner. The as-synthesized HsGDY exhibits outstanding catalytic performance towards electrochemical nitrogen reduction reaction, as demonstrated by the highly competitive yield of 103 µg h⁻¹ mg⁻¹_{cat} and potential of -0.2 V, which is comparable or even better than noble metal and the top-level single-atom catalysts. The inner alkynyl carbon atom in the defective HsGDY is identified as the active site, whose activity is triggered by the slight O doping in the form of C=O at the outer alkynyl C. Our work represents a remarkable progress in synthesizing 2D crystalline HsGDY and further highlights its enormous potentials in catalysis and other research fields.

SUPPLEMENTAL INFORMATION

Supplemental Information can be found online.

ACKNOWLEDGMENTS

This research is funded in Hong Kong by GRF Scheme under Project CityU 11305218 and the Science Technology and Innovation Committee of Shenzhen Municipality (Grant No. JCYJ20170818103435068), in USA by National Science Foundation-Centers of Research Excellence in Science and Technology (NSF-CREST Center) for Innovation, Research and Education in Environmental Nanotechnology (CIRE2N) (Grant No. HRD-1736093).

AUTHOR CONTRIBUTIONS

Conceptualization: Q.Y., Y.G., and C.Y.Z.; Methodology: Q.Y., Y.G., Z.X.L., and C.Y.Z.; Investigation, Q.Y., X.L.L., Z.D.H., and S.Y. X.; Computation: J.X.G. and N.L.; Writing-Original Draft: Q.Y.; Writing-Review &Editing, Q.Y., J.F., Z. C., and C.Y.Z.; Supervision, J.S.Q., Y.L.L., Z. C., and C.Y.Z.

REFERENCES

- 1. G. Li, Y. Li, H. Liu, Y. Guo, Y. Li and D. Zhu, Chem. Commun. 46 (2010) 3256-3258.
- 2. R. H. Baughman, H. Eckhardt and M. Kertesz, J. Chem. Phys. 87 (1987) 6687-6699.
- 3. C. Huang, Y. Li, N. Wang, Y. Xue, Z. Zuo, H. Liu and Y. Li, Chem. Rev. 118 (2018) 7744-7803.
- 4. Y. Li, L. Xu, H. Liu and Y. Li, Chem. Soc. Rev. 43 (2014) 2572-2586.
- 5. X. Gao, H. Liu, D. Wang and J. Zhang, Chem. Soc. Rev. 48 (2019) 908-936.
- Y. Zhao, J. Wan, H. Yao, L. Zhang, K. Lin, L. Wang, N. Yang, D. Liu, L. Song,
 J. Zhu, L. Gu, L. Liu, H. Zhao, Y. Li and D. Wang, Nat. Chem. 10 (2018) 924-931.
- 7. Z. Zuo and Y. Li, Joule 3 (2019) 899-903.
- 8. H. Yan, S. Guo, F. Wu, P. Yu, H. Liu, Y. Li and L. Mao, Angew. Chem., Int. Ed. 57 (2018) 3922-3926.
- 9. S. Li, Y. Chen, H. Liu, Y. Wang, L. Liu, F. Lv, Y. Li and S. Wang, Chem. Mater. 29 (2017) 6087-6094.
- 10. Z. Jia, Y. Li, Z. Zuo, H. Liu, C. Huang and Y. Li, Acc. Chem. Res. 50 (2017) 2470-2478.
- 11. J. He, N. Wang, Z. Cui, H. Du, L. Fu, C. Huang, Z. Yang, X. Shen, Y. Yi, Z. Tu and Y. Li, Nat. Commun. 8 (2017) 1172.
- 12. Q. Lv, W. Si, J. He, L. Sun, C. Zhang, N. Wang, Z. Yang, X. Li, X. Wang, W. Deng, Y. Long, C. Huang and Y. Li, Nat. Commun. 9 (2018) 3376.
- 13. N. Wang, J. He, K. Wang, Y. Zhao, T. Jiu, C. Huang and Y. Li, Adv. Mater. 31 (2019) 1803202.
- 14. S. Zhuo, Y. Shi, L. Liu, R. Li, L. Shi, D. H. Anjum, Y. Han and P. Wang, Nat. Commun. 9 (2018) 3132.
- 15. W. Zhou, H. Shen, C. Wu, Z. Tu, F. He, Y. Gu, Y. Xue, Y. Zhao, Y. Yi, Y. Li and Y. Li, J. Am. Chem. Soc. 141 (2019) 48-52.
- 16. S. L. Foster, S. I. P. Bakovic, R. D. Duda, S. Maheshwari, R. D. Milton, S. D. Minteer, M. J. Janik, J. N. Renner and L. F. Greenlee, Nat. Catal. 1 (2018) 490-500.
- 17. C. Ling, X. Niu, Q. Li, A. Du and J. Wang, J. Am. Chem. Soc. 140 (2018) 14161-14168.
- 18. Y. Luo, G.-F. Chen, L. Ding, X. Chen, L.-X. Ding and H. Wang, Joule 3 (2019) 279-289.

- 19. N. Cao, Z. Chen, K. Zang, J. Xu, J. Zhong, J. Luo, X. Xu and G. Zheng, Nat. Commun. 10 (2019) 2877.
- 20. L. Zhang, X. Ji, X. Ren, Y. Ma, X. Shi, Z. Tian, A. M. Asiri, L. Chen, B. Tang and X. Sun, Adv. Mater. 30 (2018) 1800191.
- 21. Y. Ren, C. Yu, X. Tan, X. Han, H. Huang, H. Huang and J. Qiu, Small Methods 3 (2019) 1900474.
- 22. H. Jin, L. Li, X. Liu, C. Tang, W. Xu, S. Chen, L. Song, Y. Zheng and S.-Z. Qiao, Adv. Mater. 31 (2019) 1902709.
- 23. Z. Sun, R. Huo, C. Choi, S. Hong, T.-S. Wu, J. Qiu, C. Yan, Z. Han, Y. Liu, Y.-L. Soo and Y. Jung, Nano Energy 62 (2019) 869-875.
- 24. V. W.-W. Yam, Acc. Chem. Res. 35 (2002) 555-563.
- 25. G. Kresse and J. Furthmüller, Comput. Mater. Sci. 6 (1996) 15-50.
- 26. P. E. Blöchl, Phys. Rev. B 50 (1994) 17953-17979.
- 27. J. P. Perdew, K. Burke and M. Ernzerhof, Phys. Rev. Lett. 77 (1996) 3865-3868.
- 28. Z. Zuo, D. Wang, J. Zhang, F. Lu and Y. Li, Adv. Mater. 31 (2019) 1803762.
- 29. C. Hu, H. Liu, Y. Liu, J.-F. Chen, Y. Li and L. Dai, Nano Energy 63 (2019) 103874.
- 30. Q. Yang, Y. Guo, B. Yan, C. Wang, Z. Liu, Z. Huang, Y. Wang, Y. Li, H. Li, L. Song, J. Fan and C. Zhi, Adv. Mater. 32 (2020) 2001755.
- 31. J. Wang, S. Zhang, J. Zhou, R. Liu, R. Du, H. Xu, Z. Liu, J. Zhang and Z. Liu, Phys. Chem. Chem. Phys. 16 (2014) 11303-11309.
- 32. N. Wang, J. He, Z. Tu, Z. Yang, F. Zhao, X. Li, C. Huang, K. Wang, T. Jiu, Y. Yi and Y. Li, Angew. Chem., Int. Ed. 56 (2017) 10740-10745.
- 33. H. Yu, Y. Xue and Y. Li, Adv. Mater. 31 (2019) 1803101.
- 34. T. Elzein, M. Nasser-Eddine, C. Delaite, S. Bistac and P. Dumas, J. Colloid Interface Sci. 273 (2004) 381-387.
- 35. J. Li, S. Li, Q. Liu, C. Yin, L. Tong, C. Chen and J. Zhang, Small 15 (2019) 1805344.
- 36. S. Wu, G. Wen, R. Schlögl and D. S. Su, Phys. Chem. Chem. Phys. 17 (2015) 1567-1571.
- 37. J. Zhong, J. Wang, J.-G. Zhou, B.-H. Mao, C.-H. Liu, H.-B. Liu, Y.-L. Li, T.-K. Sham, X.-H. Sun and S.-D. Wang, J. Phys. Chem. C 117 (2013) 5931-5936.
- 38. C.-H. Chuang, S. C. Ray, D. Mazumder, S. Sharma, A. Ganguly, P. Papakonstantinou, J.-W. Chiou, H.-M. Tsai, H.-W. Shiu, C.-H. Chen, H.-J. Lin, J. Guo and W.-F. Pong, Sci. Rep. 7 (2017) 42235.
- 39. B. M. Hoffman, D. Lukoyanov, Z.-Y. Yang, D. R. Dean and L. C. Seefeldt, Chem. Rev. 114 (2014) 4041-4062.
- 40. T. He, P. Pachfule, H. Wu, Q. Xu and P. Chen, Nat. Rev. Mater. 1 (2016) 16059.
- 41. T. Wu, H. Zhao, X. Zhu, Z. Xing, Q. Liu, T. Liu, S. Gao, S. Lu, G. Chen, A. M. Asiri, Y. Zhang and X. Sun, Adv. Mater. (2020) 2000299.
- 42. L. Xia, J. Yang, H. Wang, R. Zhao, H. Chen, W. Fang, A. M. Asiri, F. Xie, G. Cui and X. Sun, Chem. Commun. 55 (2019) 3371-3374.
- 43. S. Z. Andersen, V. Čolić, S. Yang, J. A. Schwalbe, A. C. Nielander, J. M. McEnaney, K. Enemark-Rasmussen, J. G. Baker, A. R. Singh, B. A. Rohr, M.

- J. Statt, S. J. Blair, S. Mezzavilla, J. Kibsgaard, P. C. K. Vesborg, M. Cargnello, S. F. Bent, T. F. Jaramillo, I. E. L. Stephens, J. K. Nørskov and I. Chorkendorff, Nature 570 (2019) 504-508.
- 44. C. Lv, C. Yan, G. Chen, Y. Ding, J. Sun, Y. Zhou and G. Yu, Angew. Chem., Int. Ed. 57 (2018) 6073-6076.
- 45. Y. Guo, T. Wang, Q. Yang, X. Li, H. Li, Y. Wang, T. Jiao, Z. Huang, B. Dong, W. Zhang, J. Fan and C. Zhi, ACS Nano (2020) DOI: 10.1021/acsnano.0c04284.
- 46. L. Xia, B. Li, Y. Zhang, R. Zhang, L. Ji, H. Chen, G. Cui, H. Zheng, X. Sun, F. Xie and Q. Liu, Inorg. Chem. 58 (2019) 2257-2260.
- 47. C. Tang and S.-Z. Qiao, Chem. Soc. Rev. 48 (2019) 3166-3180.
- 48. Y. Yao, S. Zhu, H. Wang, H. Li and M. Shao, J. Am. Chem. Soc. 140 (2018) 1496-1501.
- 49. X. Yu, P. Han, Z. Wei, L. Huang, Z. Gu, S. Peng, J. Ma and G. Zheng, Joule 2 (2018) 1610-1622.
- 50. X. Yang, K. Li, D. Cheng, W.-L. Pang, J. Lv, X. Chen, H.-Y. Zang, X.-L. Wu, H.-Q. Tan, Y.-H. Wang and Y.-G. Li, J. Mater. Chem. A 6 (2018) 7762-7769.
- 51. G.-F. Chen, X. Cao, S. Wu, X. Zeng, L.-X. Ding, M. Zhu and H. Wang, J. Am. Chem. Soc. 139 (2017) 9771-9774.
- 52. Y. Zhang, W. Qiu, Y. Ma, Y. Luo, Z. Tian, G. Cui, F. Xie, L. Chen, T. Li and X. Sun, ACS Catal. 8 (2018) 8540-8544.
- 53. M.-M. Shi, D. Bao, B.-R. Wulan, Y.-H. Li, Y.-F. Zhang, J.-M. Yan and Q. Jiang, Adv. Mater. 29 (2017) 1606550.
- 54. Y. Wang, X. Cui, J. Zhao, G. Jia, L. Gu, Q. Zhang, L. Meng, Z. Shi, L. Zheng, C. Wang, Z. Zhang and W. Zheng, ACS Catal. 9 (2019) 336-344.
- 55. C. Li, J. Yu, L. Yang, J. Zhao, W. Kong, T. Wang, A. M. Asiri, Q. Li and X. Sun, Inorg. Chem. 58 (2019) 9597-9601.
- 56. C. Li, D. Ma, S. Mou, Y. Luo, B. Ma, S. Lu, G. Cui, Q. Li, Q. Liu and X. Sun, J. Energy Chem. 50 (2020) 402-408.
- W. Zang, T. Yang, H. Zou, S. Xi, H. Zhang, X. Liu, Z. Kou, Y. Du, Y. P. Feng,
 L. Shen, L. Duan, J. Wang and S. J. Pennycook, ACS Catal. 9 (2019) 10166-10173.
- 58. X. Wang, W. Wang, M. Qiao, G. Wu, W. Chen, T. Yuan, Q. Xu, M. Chen, Y. Zhang, X. Wang, J. Wang, J. Ge, X. Hong, Y. Li, Y. Wu and Y. Li, Sci. Bull. 63 (2018) 1246-1253.